Physics of Plasmas

Mildly relativistic collisionless shock formed by magnetic piston

Cite as: Phys. Plasmas **27**, 122106 (2020); https://doi.org/10.1063/1.5144683
Submitted: 09 January 2020 . Accepted: 14 November 2020 . Published Online: 16 December 2020

Q. Moreno, A. Araudo, Ph. Korneev, C. K. Li, V. T. Tikhonchuk, X. Ribeyre, E. d'Humières, and S. Weber

Physics of Plasmas ARTICLE scitation.org/journal/php

Mildly relativistic collisionless shock formed by magnetic piston

Cite as: Phys. Plasmas **27**, 122106 (2020); doi: 10.1063/1.5144683
Submitted: 9 January 2020 · Accepted: 14 November 2020 ·
Published Online: 16 December 2020

Q. Moreno,[1,a)] A. Araudo,[1,2] Ph. Korneev,[3,4] C. K. Li,[5] V. T. Tikhonchuk,[1,6] X. Ribeyre,[6] E. d'Humières,[6] and S. Weber[1,7]

AFFILIATIONS

[1]ELI-Beamlines, Institute of Physics, Czech Academy of Sciences, 25241 Dolní Břežany, Czech Republic
[2]Astronomical Institute, Czech Academy of Sciences, 141 00 Prague, Czech Republic
[3]National Research Nuclear University "MEPhI," 115409 Moscow, Russian Federation
[4]P. N. Lebedev Physical Institute, Russian Academy of Sciences, 119991 Moscow, Russian Federation
[5]Plasma Science and Fusion Center, Massachusetts Institute of Technology, Cambridge, Massachusetts 02139, USA
[6]Centre Lasers Intenses et Applications, University of Bordeaux, CNRS, CEA, 33405 Talence, France
[7]School of Science, Xian Jiaotong University, Xian 710049, China

[a)]**Author to whom correspondence should be addressed:** Quentin.Moreno@eli-beams.eu

ABSTRACT

By using particle-in-cell simulations, we study the collision of two plasma flows with one of them carrying a magnetic field. Ion interpenetration results in the formation of a magnetic piston with the magnetic field compression proportional to the density ratio of the colliding plasmas. The counterpropagating ions in the nonmagnetized plasma upstream from the piston excite the ion Weibel instability, which turns into magnetic turbulence. The thickness of the piston increases with time, and it turns into a reverse magnetized shock after less than one ion gyro period. In front of the piston, the time needed to decrease the nonmagnetized ion anisotropy using the magnetic turbulence is much larger than the ion gyroperiod in the piston. Consequently, particles are reflected by the piston, which acts as a wall initiating a transient phase. After several ion periods, the formation of this electromagnetic forward shock is, then, accelerated by the piston, and at large timescale, the dissipation of energy is eventually mediated only by the Weibel turbulence. We report here a new configuration of shocks, where a reverse magnetized and a forward electromagnetic shock coexist separated by a tangential discontinuity. Particle acceleration and heating in the two shock structures and relevance of this scenario of collisionless shock formation to laboratory experiments and astrophysical conditions are discussed.

I. INTRODUCTION

Collisionless shocks are ubiquitous in the universe and of a wide variety. Three groups of shocks have been classified regarding the magnetization level and the kinetic energy of the sources: electrostatic,[1,2] magnetized,[3] and electromagnetic,[4,5] where each of them depends on a variety of plasma instabilities necessary for shock dissipation (see Ref. 6, for a review). Electromagnetic shocks in astrophysical sources accelerate cosmic rays via the first order Fermi mechanism due to the presence of magnetic turbulence, on both sides of the shock front, confining the particles close to it.[7,8] These magnetic inhomogeneities can appear due to the nonlinear Weibel instability[9] routinely excited in a homogeneous plasma, which possesses an anisotropy in momentum space (e.g., Refs. 10 and 11).

Electromagnetic shocks have been an important subject of investigation in astrophysics and laboratory plasmas,[12] but, in contrast to electrostatic[13] or magnetized shocks,[14] the formation conditions are difficult to reach on current laser facilities since they require hot (∼keV) and fast plasma flows ($>1000\,\mathrm{km\,s^{-1}}$) on several nanosecond timescale. The most explored experimental route for their formation consists of colliding two ablative unmagnetized flows driven by high-energy nanosecond lasers, which yielded promising results like the formation of magnetic filaments.[15–17] However, this method did not successfully demonstrate the shock formation, which requires longer time scales. It is, therefore, very timely to investigate other configurations of plasma interaction likely to form electromagnetic shocks on a spatio-temporal scale accessible in the laboratory.[18]

Astrophysical jets may produce shocks in their interaction with an external medium. The jet termination region presents a double shock structure (working surface) where the forward and reverse shocks are separated by a contact discontinuity. The physical mechanisms leading to the formation of these shocks cannot be assessed only from the emission produced in the shock downstream region. Numerical simulations and laboratory experiments contribute to better understanding of this complex phenomenon. For instance, Dieckmann *et al.* presented a numerical study of the formation of termination shocks in unmagnetized relativistic pair jets propagating in a cool ambient magnetized plasma composed of electrons and protons.[19]

Relativistic jets in gamma ray bursts, active galactic nuclei (e.g., M87), microquasars (e.g., SS433), and nonrelativistic jets in protostars (e.g., HH-47[20]) usually carry their own magnetic field. The jet magnetic field near the launching region is large enough to accelerate and collimate the plasma but becomes dynamically insignificant far from the central source where termination shocks are observed. However, even when the magnetic field is not large enough to magnetize the ions, it can magnetize the electrons that are much lighter. The magnetic field in the external medium is often much lower than the one carried by the jet at the interaction point, leading to early interaction behavior like adiabatic compression as discussed in the present paper, which paves the way to several instabilities and shock formation.

In order to study the formation and evolution of double-shock structures seen in the termination region of astrophysical jets, we perform a numerical study of a mildly relativistic magnetized plasma moving in an unmagnetized ambient medium. The magnetic field in the jet plasma is chosen perpendicular in order to forbid the growth of the modified-two-stream instability, among others.[21] However, this geometry may efficiently allow us also to speed up the formation of the shocks, thus presenting a novel approach to experimental studies for the collisionless shock formation.

Note that a perpendicular regular magnetic field has been recently reported in Ref. 22 in the jet of the microquasar SS433 with the jet velocity of $\sim 0.2c$. Such a magnetic field was also identified in the laboratory experiment[18] where it was proposed as a reason for accelerated shock formation.

We present 2D particle-in-cell (PIC) simulations leading to a double-shock structure composed of a fast magnetosonic reverse shock and an electromagnetic forward shock mediated by Weibel turbulence. Our paper is structured as follows. Section II summarizes the numerical method of the PIC simulation code that we use and the initial conditions. Sections III and IV present the simulation results concerning the plasma expansion phase and shock formation.

Section V is devoted to a discussion on particle acceleration and heating and the effect of the reduced mass ratio, and finally, the conclusions are presented in Sec. VI. MKS units are used all along the paper.

II. THE PIC CODE AND THE INITIAL CONDITIONS

We use the PIC simulation code PICLS.[23] The code is based on the directional splitting scheme, which solves the electromagnetic fields on a single computational grid.[24] The plasma is approximated by an ensemble of computational particles (CPs). The momentum of each CP is updated via a discretized form of the Lorentz force equation, which uses the electromagnetic field values that have been interpolated from the numerical grid to the position of the CP. We resolve two spatial dimensions and the three velocity components of the CP (2D3V). In the simulations, the time and space dimensions are normalized to $1/\omega_{pe}$ and c/ω_{pe}, respectively, where ω_{pe} is the electron plasma frequency. The electric and magnetic fields are normalized to their reference field $E_r = m_e c\omega_{pe}/e$ and $B_r = m_e\omega_{pe}/e$, respectively. This normalization makes our study relevant from the astrophysical to the laboratory scale, according to the scaling laws.[25]

We perform a two-dimensional simulation in a box $[L_x, L_y] = [2052, 504]\ c/\omega_{pe}$ aligned with the x-y plane and subdivided into grid cells $[\Delta_x, \Delta_y] = 0.5\ c/\omega_{pe}$. All boundaries are periodic for the fields, and for the particles, they are periodic in the transverse direction y and absorbing in the x-direction. The simulation is initialized with Maxwellian velocity distributions for electrons and protons with 50 particles per cell and per species. A sketch of the simulation initial conditions is provided in Fig. 1.

A jet (Plasma 1) fills the interval $-1026\ c/\omega_{pe} \le x \le 0$ and moves at a velocity $v_0 = 0.2c$ from left to right along the x-axis. The electron and ion temperatures are $T_{e1} = T_{i1} = 10$ keV, and the electron and ion densities are $n_{e1} = n_{i1} = n_0$, where n_0 is a scalable arbitrary value. A magnetic field aligned with the z-axis is imposed on the jet with the strength $B_1 = 6.25 \times 10^{-2} B_r$ sufficient to magnetize the electrons. The magnetic field is maintained by the integral currents on the surface, which are created by electrons, confined by ions with the electrostatic tension. For Plasma 1, to carry the magnetic field, an electric field $E_{y1} = v_0 B_1$ is applied to the jet.

An ambient medium (Plasma 2) fills the interval $0 \le x \le 1026\ c/\omega_{pe}$, with motionless electrons and ions having temperatures and densities $T_{e2} = T_{i2} = 10$ keV and $n_{e2} = n_{i2} = n_0 R$, respectively, where $R = n_{i2}/n_{i1}$ is the ambient to jet density ratio. The indices e1/i1 and e2/i2 stand for electrons (e) and ions (i) for Plasma 1 and Plasma 2, respectively.

Table I lists all relevant parameters of the jet, where $\mu = m_i/m_e$ is the ion-to-electron mass ratio, ϵ_0 is the vacuum permittivity, and $\Gamma_e = 5/3$ and $\Gamma_i = 2$ are the adiabatic indices for electrons and ions, respectively. Their gyrofrequencies are ω_{ce} and ω_{ci}, respectively, and the lower hybrid frequency is ω_{LH}. The electron/ion's gyroradius is $r_{e,i}$. We also list the ion acoustic c_s, Alfvén v_A, and magnetosonic speeds c_{ms}, as well as the speed of the center of mass v_c between the two plasmas. The flow is supersonic when $\mu = m_i/m_e > 1$, with the acoustic Mach number $M_s = v_0/c_s \simeq \sqrt{\mu}$ and super-Alfvenic with the Alfvén Mach number $M_A = v_0/v_A \simeq 3.2\sqrt{\mu}$. We follow the jet propagation through the ambient medium during the time interval $0 \le t \le t_{\max}$ with $t_{\max} = 5 \times 10^3 \omega_{pe}^{-1} = 5 \times 10^3 \omega_{pi}^{-1}/\sqrt{\mu}$, which we resolve in 10^4 steps.

Time formation of shocks is mediated by ion instabilities, such as the ion Weibel instability. This time depends of the ion mass and can be a very long process on the electron timescale. In order to speed up the instability development and shock formation, our simulations are considering an ion-to-electron mass ratio numerically reduced from the real proton mass $\mu = 1836$ to $\mu = [1836, 200, 50, 20]$ to study subsequently longer and longer phases of the process. For this reason, we show in Table I the mass ratio μ as a free parameter. We discuss the effect of the mass ratio in Sec. V.

III. EXPANSION PHASE

A. Magnetic piston formation ($\mu = 1836$)

The early interaction phase was simulated with the real ion-to-electron mass ratio $\mu = 1836$. Figure 2 displays the magnetic field

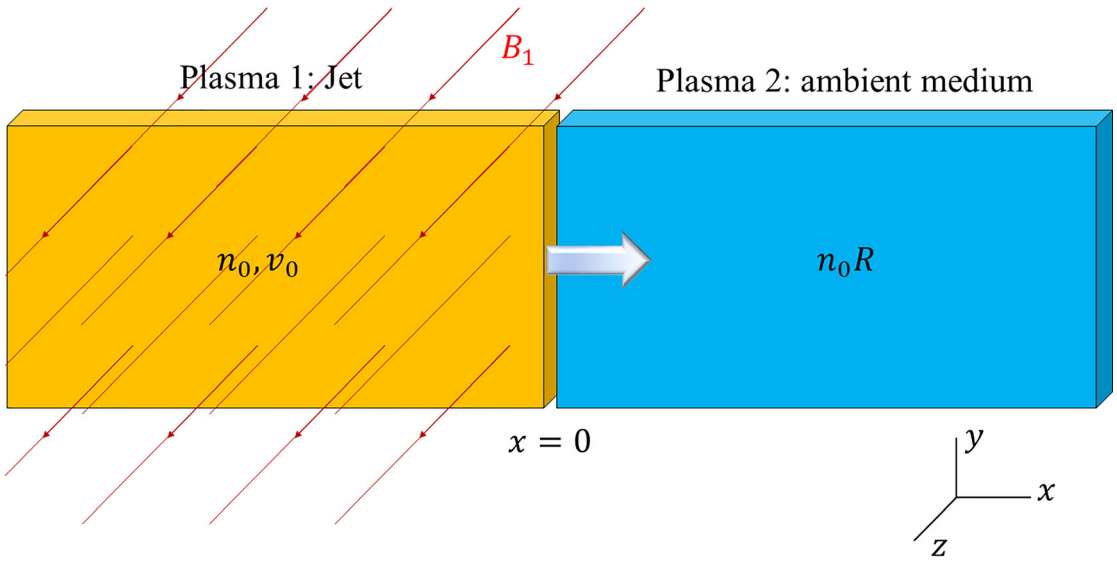

FIG. 1. Sketch of the initial plasma density distribution and magnetic field in the simulations.

amplitude and the proton density at a half of simulation time $t = t_{\max}/2 = 58\omega_{pi}^{-1}$ in the interval $-1052/\sqrt{\mu} \le x \le 1052/\sqrt{\mu}$ $c\omega_{pi}^{-1}$. At initial time, the ions of Plasma 1 are freely penetrating in Plasma 2, given that there are no collisions that can slow them down. The electrons are pulled with ions by the electrostatic field of charge separation,[26] but their motion is constrained by the magnetic field. Initially, the electron penetration depth is of the order of their Larmor radius. This, however, is sufficient for activation of the magnetic field penetration into the unmagnetized zone. Gradual accumulation of electrons in the magnetized plasma, charge neutralization, and magnetic field compression lead eventually to the displacement of the magnetic field edge in the direction of ion flow but with a velocity $v_B = v_c$ smaller than v_0. It propagates in a form of magnetic piston.

The magnetic piston is defined on the kinetic scales of electron skin depth ($c.\omega_{pe}^{-1}$), Larmor radius, and inertia length. On larger hydrodynamical scales, the jump conditions between regions 1, 2, 3, and 4, introduced in Fig. 2, and the magnetic front velocity are defined by the conservation laws as follows:

TABLE I. The initial conditions selected for the plasma jet and the definitions of the relevant plasma parameters for an unknown density n_0 and unknown μ. The jet velocity is $v_0 = 0.2c$ (i.e., $\gamma_0 = 1.02$), the magnetic field strength is $B_1 = 6.25 \cdot 10^{-2} B_r$, $T_{e,i} = 10$ keV, and $Z = 1$.

Parameter	Initial value
$\omega_{pe} = (n_0 e^2/\epsilon_0 m_e)^{1/2}$	Arbitrary
$\omega_{ce} = eB_1/m_e$	$6.28 \times 10^{-2}\,\omega_{pe}$
$\omega_{pi} = (n_i Z^2 e^2/\epsilon_0 m_i)^{1/2}$	$1/\sqrt{\mu}\,\omega_{pe}$
$\omega_{ci} = eZB_1/m_i$	$1/\mu \times 6.28 \times 10^{-2}\,\omega_{pe}$
$\omega_{LH} = ((\omega_{ce}\omega_{ci})^{-1} + \omega_{pi}^{-2})^{-1/2}$	$1/\sqrt{\mu} \times 6.26 \times 10^{-2}\,\omega_{pe}$
$r_e = v_0/\omega_{ce}$	$3.1\,c.\omega_{pe}^{-1}$
$r_i = v_0/\omega_{ci}$	$\mu \times 3.1\,c.\omega_{pe}^{-1}$
$c_s = ((\Gamma_e T_e + \Gamma_i T_i)/m_i)^{1/2}$	$1/\sqrt{\mu} \times 2.7 \times 10^{-1} c$
$v_a = B_1/(\mu_0 n_0 m_i)^{1/2}$	$1/\sqrt{\mu} \times 6.2 \times 10^{-2} c$
$c_{ms} = (v_a^2 + c_s^2)^{1/2}$	$1/\sqrt{\mu} \times 2.5 \times 10^{-1} c$
$v_c = v_0/(1+R)$	$10^{-1} c$
$\beta = (c_s/v_a)^2$	~ 18

- Density: The charge conservation implies that the electron density in the plasma overlapping regions 3 and 4 is equal to the ion density, that is,

$$n_{e3} = n_{e4} = n_{i1} + n_{i2} = (1+R)n_0. \quad (1)$$

- Magnetic field: As the electrons are magnetized, the magnetic field in a continuous flow is proportional to the electron density, giving $B/n_e = \text{const}$,[27]

$$B_3 = B_1 \frac{n_{e3}}{n_{e1}} = (1+R)B_1. \quad (2)$$

- Velocity: The magnetic flux is conserved, that is, the product of the magnetic field and the electron flow velocity is also conserved, and then, the velocity of the magnetic front propagation reads

$$v_B = v_0 \frac{B_1}{B_3} = \frac{v_0}{1+R}. \quad (3)$$

- Temperature: Electron adiabatic compression increases the electron temperature. In a magnetized plasma, this effect corresponds to the conservation of the electron magnetic invariant,

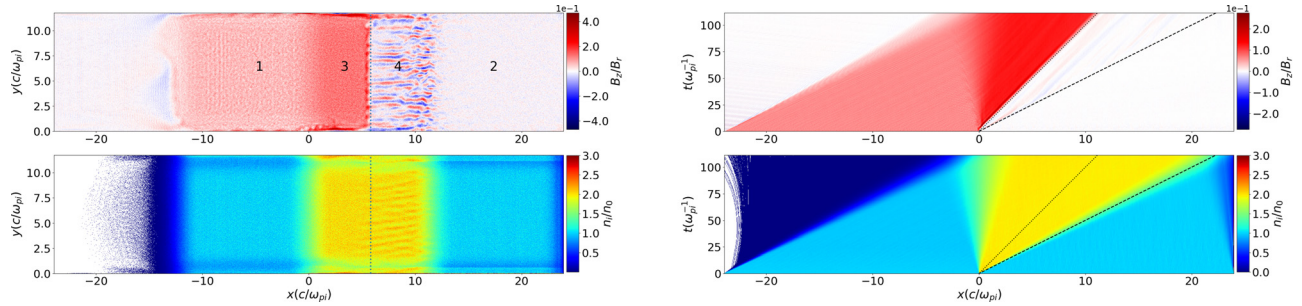

FIG. 2. Magnetic field (top) and ion density (bottom, clamped at 3 for visualization reasons) at time $t = t_{max}/2 = 58\omega_{pi}^{-1}$ (left) and their evolution with time (right). In the top left panel, zones 1 and 2 correspond to Plasma 1 and Plasma 2, respectively, whereas 3 and 4 are the compressed zones of Plasma 1 and Plasma 2, respectively. The speeds v_c and v_0 are overplotted by dotted and dashed lines, respectively. The mass ratio is $\mu = 1836$, and the density ratio is $R = 1$.

$\mu_e = m_e v_\perp^2/2B$, where $v_\perp^2 = \tilde{v}_x^2 + \tilde{v}_y^2$ is the electron rotational velocity in the plane perpendicular to the magnetic field direction, where $\tilde{v}_{x,y} = v_{x,y} - \langle v_{x,y}\rangle_t$ and $\langle v\rangle_t$ is a "slow" time-averaged motion.[28] Consequently, compression of the magnetic field by a factor $1 + R$ implies an increase in the electron transverse velocity, which corresponds to the transverse temperature $T_\perp = m_e v_\perp^2/2$, by the same factor,

$$T_{e3\perp} = T_{e1\perp}\frac{B_3}{B_1} = (1+R)T_{e1\perp}. \tag{4}$$

As the electron average energy in the magnetic field direction remains unchanged, the electron distribution becomes anisotropic and the effective temperature in region 3 increases by a factor of $1 + 2R/3$,

$$T_{e3} = \frac{1}{3}T_{e1\|} + \frac{2}{3}T_{e3\perp} = \left(1 + \frac{2}{3}R\right)T_{e1}. \tag{5}$$

These estimates for the parameters upstream and downstream of the magnetic field discontinuity are in good agreement with 2D3V numerical simulations shown in Fig. 2.

A dependence of the magnetic field compression on the plasma density ratio is studied in more detail with 1D PIC simulations performed with the code EPOCH.[29,30] Figure 3(a) shows the details of the adiabatic compression at the edge of immobile plasma 2 ($x = 0$). The formal discontinuity is in reality a smooth transition on the electron spatial scale. It begins with a width of a few electron Larmor radii and then gradually widens because of the magnetic field diffusion. This process can also be considered as a propagation of finite amplitude magnetosonic waves to the right in plasma 2 and to the left in plasma

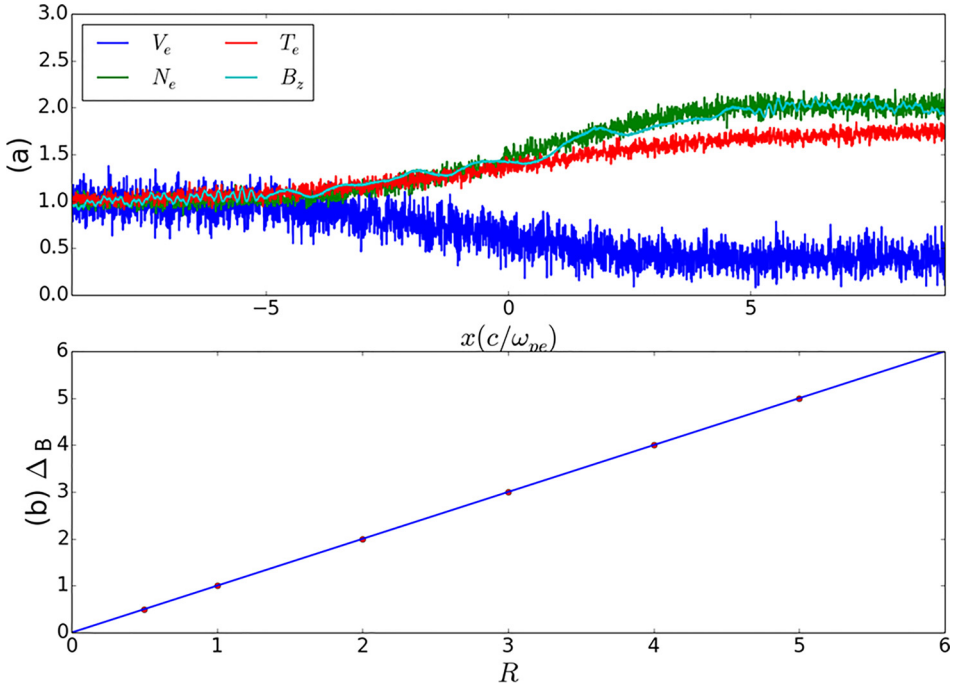

FIG. 3. Top: detailed view of the shock discontinuity between regions 1 and 3, at time $58\omega_{pi}^{-1}$ for the density ratio $R = 1$ and $\mu = 1836$. Bottom: dependence of the magnetic field jump $\Delta_B = B_3/B_1$ on the density ratio $R = n_{i2}/n_{i1}$.

1. A linear dependence of the magnetic field compression on the plasma density ratio is shown in Fig. 3 (bottom).

Slowing down of the magnetized electron fluid compared to the ion flow implies that there are two ion streams in zone 4 free of magnetic field: the ions of Plasma 2 and the ions of Plasma 1 moving at a high velocity ($v_0 > v_B$). This ion anisotropy characterized by the parameter

$$a_s = \frac{K_{s,x}}{K_{s,y}} - 1, \quad K_{s,x/y} = m_i v_{s,x/y}^2 + T_{s,x/y} \tag{6}$$

is prone to excitation of the ion Weibel instability as illustrated in Fig. 2, where $T_{s,x}$ and $T_{s,y}$ are the longitudinal and transverse temperatures of the sth plasma species, respectively. In the center of mass reference frame, the growth rate δ of the ion Weibel instability has been estimated in the nonrelativistic regime for hot electrons ($\delta \ll k v_{th}$) in Ref. 31 and takes the following expression:

$$\delta \simeq \sqrt{\frac{2T_{iy}}{\pi m_i}} |k_y| \frac{k_{max}^2 c^2 - k_y^2 c^2}{k_{max}^2 c^2}, \tag{7}$$

where

$$k_{max} \simeq \frac{\omega_{pi}}{c} \sqrt{a_i}, \tag{8}$$

is the upper limit of the Weibel domain, considering here a zero electron anisotropy. The maximum growth rate is found to be $\delta_{max} \propto \omega_{pi}(v_0 - v_c)/c$ in the limit $v_{Ti} \ll v_0$, for a wavenumber $k_{sat} \simeq k_{max}/\sqrt{3}$. These estimations are in agreement with the simulation results. Saturation of the instability is due to the ion trapping mechanism,[32] which occurs at time $\tau_{sat} \simeq \delta_{max}^{-1}$.

Adiabatic compression in zone 3 results in formation of a magnetic piston where its strength and velocity are defined by the initial density ratio R, and its reduced velocity compared to the plasma flow allows the growth of the Weibel instability on its front in zone 4. The Weibel mediated shock is expected to form on a much larger spatiotemporal scale after the instability saturation. Such a time is unreachable in PIC simulations with a real proton-to-electron mass ratio.[33] In order to investigate the effect of the magnetic piston on the shock formation, we perform 2D PIC simulations, in the same setup as in Sec. II, but with lower mass ratio $\mu < 1836$ and $R = 1$.

B. Weibel saturation, ion rotation, and initial transient phase ($\mu = 200$)

Simulation with a lower mass ratio $\mu = 200$ allows us to extend the time of plasma evolution by more than three times. Figure 4 (left) displays the magnetic field amplitude and the proton density at the end of simulation $t = t_{max} = 354\omega_{pi}^{-1}$ in the interval $-1052/\sqrt{\mu} \le x \le 1052/\sqrt{\mu}\, c\omega_{pi}^{-1}$.

In compressed region 3, the magnetic field strength has increased from B_1 to $B_3 = B_1(1 + R)$. The convected electric field $E_{y1} = v_0 B_1$ carried by the magnetized electrons from Plasma 1 remains unchanged during the adiabatic compression according to Eqs. (2) and (3). As a consequence, ions from Plasma 1 and Plasma 2 are accelerated in opposite directions,

$$\frac{dv_{y1}}{dt} = \frac{e}{m_i}(E_{y1} - v_0 B_3) = -\frac{e}{m_i} v_0 B_1 R \tag{9}$$

and

$$\frac{dv_{y2}}{dt} = \frac{e}{m_i} E_{y1} = \frac{e}{m_i} v_0 B_1, \tag{10}$$

when penetrating the compressed region. This acceleration results in a compression of ions in region 3. The magnetized electrons are compressed with ions by the electrostatic field of charge separation, and this process leads to further enhancement of the magnetic field strength. Transverse ion acceleration and magnetic field compression are shown in Fig. 5(c). The density of Plasma 2 in the magnetic piston is ~3.7, while Plasma 1 reaches a local density higher than 7. Ions from Plasma 1 perform their Larmor rotation in compressed region 3, and they will be longitudinally decelerated and eventually stopped at

$$t_p \simeq \frac{\pi}{(1 + R)\omega_{ci}} = \pi \frac{B_r}{B_3} \sqrt{\mu}\, \omega_{pi}^{-1}. \tag{11}$$

Figure 4 (right) shows the ion density and the magnetic field compression at $t \sim 350\omega_{pi}^{-1} \sim t_p$.

After the Weibel instability nonlinear saturation in region 4, magnetic filaments coalesce and form a turbulence with the magnetic spectrum shifted to larger wavelengths $\lambda_y \simeq 3\lambda_{sat} = 3(2\pi/k_{sat})$ corresponding to ~10 ion skin depth [cf. Figs. 5(a) and 5(b)]. This process is accompanied by transverse ion heating [cf. Figs. 5(d) and 5(e)], which is a necessary element for dissipation of the kinetic energy of

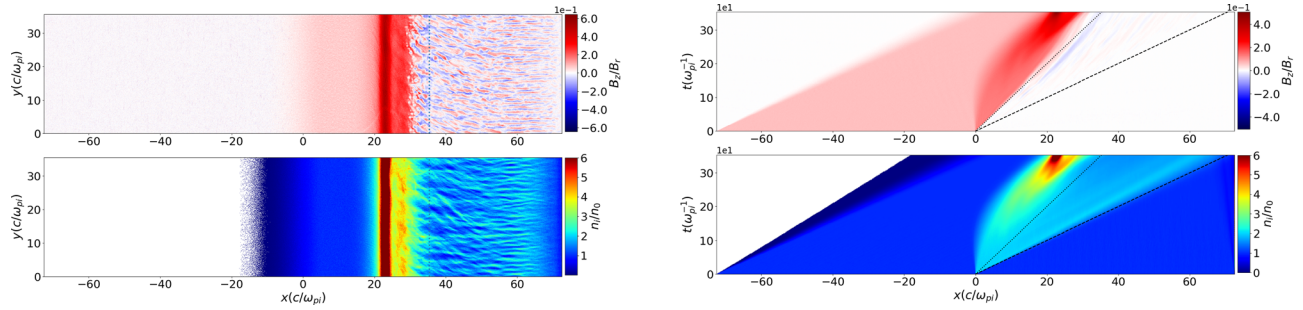

FIG. 4. Magnetic field (top) and ion density (bottom, clamped at 6 for visualization reasons) at time $t = t_{max} = 354\omega_{pi}^{-1}$ (left) and their evolution with time (right). The speeds v_c and v_0 are overplotted by dotted and dashed lines, respectively. The mass ratio is $\mu = 200$.

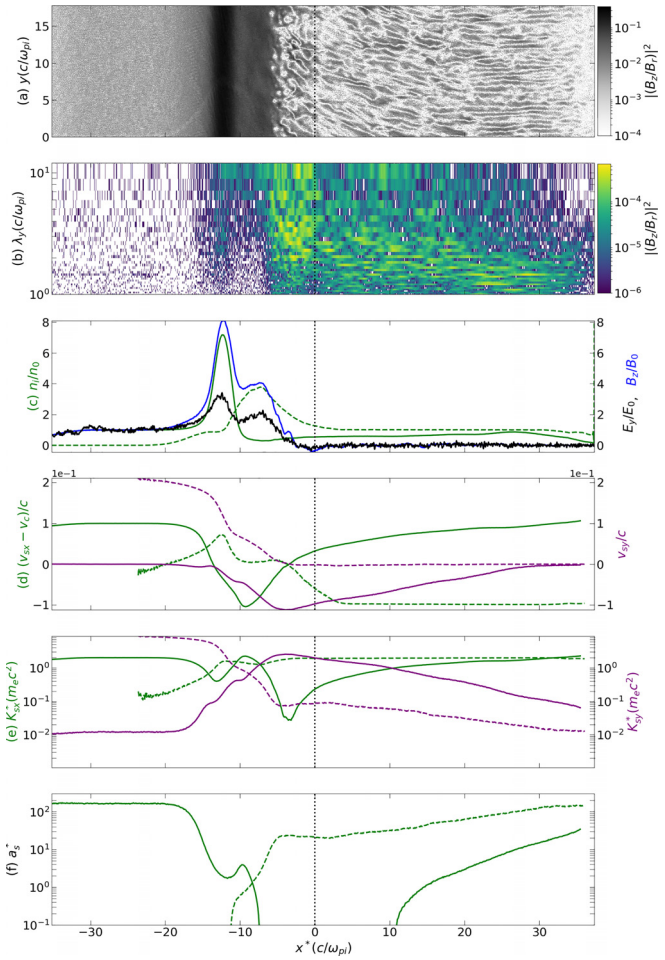

FIG. 5. (a) and (b) The magnetic energy density and its spectrum, respectively. (c) The ion density (green), magnetic field (blue), and electric field (black) averaged over the *y*-axis. (d) The mean velocity of each ion species, (e) their kinetic energy (green: v_x and K_x and purple: v_y and K_y) and (f) the ion anisotropy. Solid lines correspond to *i*1 and the dashed lines to *i*2. The mass ratio is $\mu = 200$, the time $t = t_{\max} = 354\omega_{pi}^{-1}$, and the reference frame is the center of mass $x^* = x - v_c t$. The vertical dotted line shows the position $x_c = v_c t$.

ion flows for the electromagnetic shock formation. The merged ion filaments in front of the magnetic piston penetrate into it and undergo transverse acceleration and bending. Furthermore, the wavelength of the filaments grows to even larger $\lambda_y \simeq 8\lambda_{\text{sat}}$ after crossing the piston boundary.

The Weibel mediated shock is expected to form at the distance[34]

$$L_{\text{iso}} \simeq 35\left(\frac{\mu}{Z_i}\right)^{0.4}\frac{c}{\omega_{pi}}, \tag{12}$$

after the time

$$t_{\text{W}} \simeq \frac{L_{\text{iso}}}{v_c} \simeq 35\frac{c}{v_c}\left(\frac{\mu}{Z_i}\right)^{0.4}\omega_{pi}^{-1}. \tag{13}$$

However, in the present simulation for $\mu = 200$, the required time for the shock formation $t_{\text{W}} \simeq 2914\omega_{pi}^{-1}$ is yet much larger than the simulation time $t_{\max} = 354\omega_{pi}^{-1}$. The Weibel-mediated shock is assumed to be formed when the anisotropy falls down to $a_i < 1$, in the configuration with no external magnetic field.[33] In our range of parameters, the Weibel-mediated shock time formation is larger than the time needed for the ions to rotate in the piston (i.e., $t_{\text{W}} > t_{\text{p}}$). This early ion rotation decreases the flow anisotropy and will eventually speed up the electromagnetic shock formation as discussed in Sec. IV.

The anisotropy of both plasmas falls down to 0.5 at $t_{\max}$ [see Fig. 5(f)].

- Plasma 1: Ion compression formed at $r_i/\pi \sim 8c/\omega_{pi}$ results from the ion rotation in the magnetic piston. The anisotropy eventually changes the sign due to the transverse ion acceleration. This compression is the seed for a reverse magnetized shock formation (see Sec. IV A 1).
- Plasma 2: In the interval $-5c/\omega_{pi} < x^* < 30c/\omega_{pi}$, the anisotropy decreases from 140 to 20 due to filament merging and transverse ion heating. In the interval $-10c/\omega_{pi} < x^* < -5c/\omega_{pi}$, ion anisotropy a_{i2} in Plasma 2 decreases to 0.5 due to the transverse ion acceleration in the magnetic piston, which eventually reflects them. This compression initializes for a forward electromagnetic shock formation (see Sec. IV A 2).

At this time, the Weibel filaments are not yet strong enough to dissipate the kinetic energy of the upstream particles from Plasma 2. Compression of Plasma 2 presents a transient phase, where the magnetic piston contributes to the particle deceleration, acting as a rigid wall.[10] The forward shock will be formed when the density compression propagates

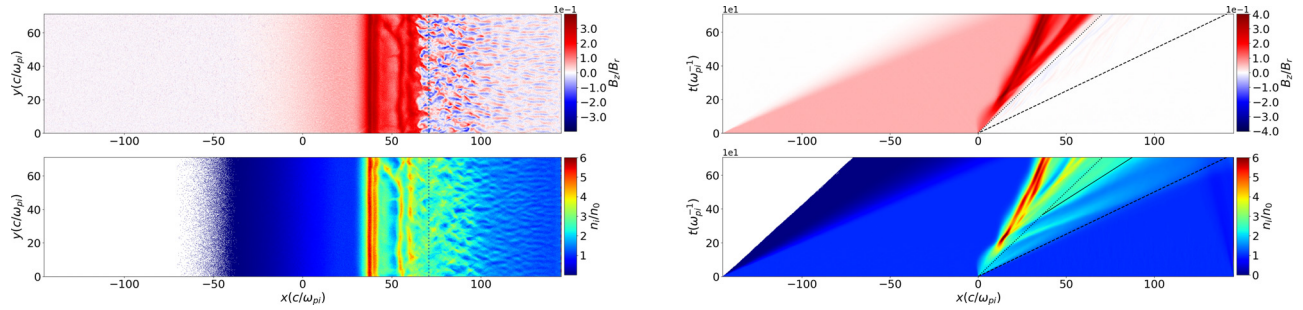

FIG. 6. Magnetic field (top) and ion density (bottom, clamped at 6 for visualization reasons) at time $t = t_{\max} = 707\omega_{pi}^{-1}$ (left) and their evolution with time (right). The speeds v_f, v_c, and v_0 are overplotted by solid, dotted, and dashed lines, respectively. The mass ratio is $\mu = 50$.

away from the magnetic piston.[10] The shock formation at a longer timescale is studied in a simulation with a smaller ion-to-electron mass ratio.

IV. SHOCK EVOLUTION

A. Early shock propagation ($\mu = 50$)

Simulation with $\mu = 50$ allows us to effectively double the time of observation of the shock evolution compared to the simulation presented in Sec. III. Figure 6 (left) displays the magnetic field amplitude and proton density at $t = t_{\max} = 707\omega_{pi}^{-1}$ in the interval $-1052/\sqrt{\mu} \le x \le 1052/\sqrt{\mu}\ c\omega_{pi}^{-1}$. Two shocks propagate in the opposite direction as shown in Fig. 6 (right).

1. Reverse shock

Compression of Plasma 1 forms a magnetized reverse shock at $t_r \simeq t_p \simeq 180\omega_{pi}^{-1}$ moving at $v_r^* = -v_0/3.5$ in the center of mass reference frame, where the index r refers to the reverse shock. The upstream velocity in the reverse shock frame is

$$v_{us}^r = |v_0 - (v_c + v_r^*)|, \tag{14}$$

leading to an acoustic Mach number $M_{s,r} = v_{us}^r/c_s = 11v_0/14c_s \simeq 0.8\sqrt{\mu} \simeq 5.7$. The shock is supercritical since the Alfvénic Mach number $M_{A,r} = v_{us}^r/v_A = 18$ is higher than the critical Mach number[35] $M_{cr} \simeq 2.39$. Density compression in the shock can be found from the MHD Rankine–Hugoniot conditions,

$$\Delta_r = \frac{2(\Gamma_i + 1)}{D + \sqrt{D^2 + 4(\Gamma_i + 1)(2 - \Gamma_i)M_{A,r}^{-2}}} \simeq 2.8, \tag{15}$$

where $D = (\Gamma_i - 1) + (2M_{s,r}^{-2} + \Gamma_i M_{A,r}^{-2})$. This value is in agreement with the plateau value of the downstream reverse shock region shown in Fig. 7 in the interval $-40c/\omega_{pi} < x^* < -6c/\omega_{pi}$.

The shock is, thus, a fast magnetosonic shock, and it moves with velocity $|v_r^*| = 1.6c_{ms}$ in the center of mass reference frame. The electrostatic potential jump at reverse shock induces a specular reflection of the fast jet ions and leads to a foot formation[36] illustrated in Figs. 7(c) and 7(d). A large supercritical Mach number allows eventually the shock to self-reform.[37] In the same way, for the case $\mu = 200$, ions from Plasma 1 provide the major contribution to the reverse shock formation.

At the time of piston formation [see Eq. (11)], the fraction of ions from Plasma 2, which have been deflected by the magnetic piston, is accelerated by the convective electric field, to the velocity $v_x = E_y/B_z$, which is even larger than the initial jet velocity v_0. This is shown in Fig. 6 (bottom right at $t = 200\omega_{pi}^{-1}$ and $x = 20c/\omega_{pi}$) and Fig. 7(e) in the interval $40 < x^* < 70c/\omega_{pi}$. Ions from Plasma 1, which succeeded to cross the magnetic piston before shock formation, join reflected ions from Plasma 2 and form an ion beam propagating through the unperturbed Plasma 2 upstream the shock, thus reducing its initial anisotropy. This is shown in the center of mass reference frame in Fig. 7(f) [$a_{i1}(x^* \to -\infty) \simeq 40 \neq a_{i2}(x^* \to \infty) \simeq 16$].

At the piston front, the two ion species continue to detach from each other, and a tangential discontinuity is formed. Its thickness is of the order of the ion Larmor radius. While the tangential discontinuity is stable over a long time in a 1D geometry,[36] it is disturbed by transverse currents as it is shown in Fig. 7(a), where large periodic modulations appear along the discontinuity. This phenomenon can be related to a magnetic mirror edge instability,[38] where transverse currents

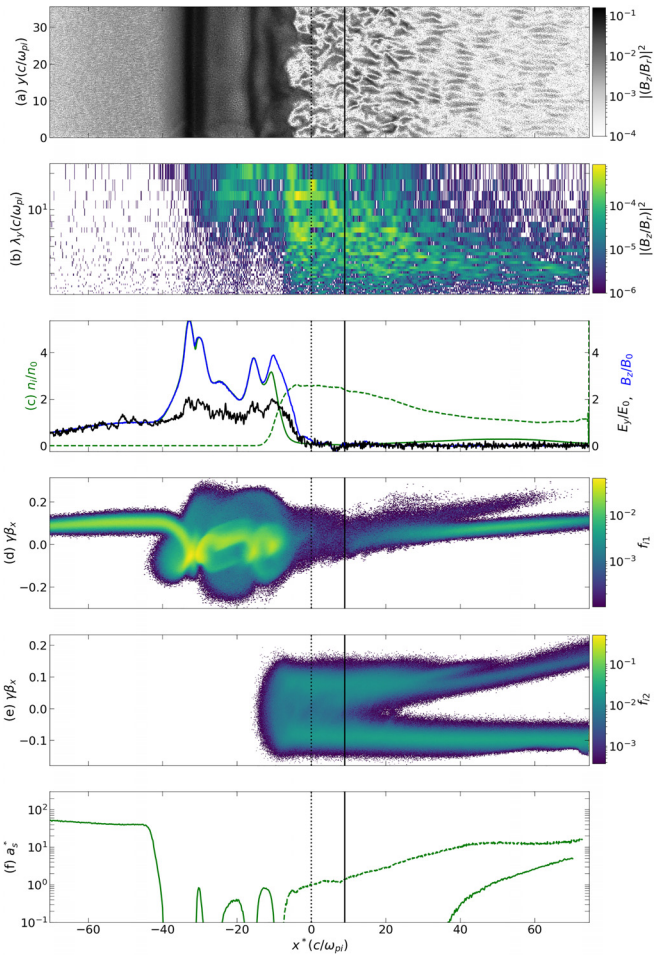

FIG. 7. (a) and (b) The magnetic energy density and its spectrum, respectively. (c) The ion density (green), magnetic field (blue), and electric field (black) averaged over the y-axis. (d) and (e) The ion phase space $\gamma\beta_x$ for $i1$ and $i2$. (f) The ion anisotropy. Solid lines correspond to $i1$ and the dashed lines to $i2$. The mass ratio is $\mu = 50$, the time $t = t_{\max} = 707\omega_{pi}^{-1}$, and the reference frame is the center of mass $x^* = x - v_c t$. Vertical dotted and solid lines show the positions $x = v_c t$ and $x = v_f(t - t_f)$, respectively.

originating from merged ion filaments continue to bend near the discontinuity, forming large magnetic bubbles of a size $\lambda_y \simeq 8\lambda_{sat}$ [cf. Figs. 9(a) and 9(b)] in the reverse shock downstream region. Due to the latter instability, the position of the discontinuity [magnetic front, blue line in Fig. 7(c)] is slightly offset compared to the position of the center of mass $x_c = v_c t$ (vertical dotted line in Fig. 7).

2. Forward shock

At the time $t_f \simeq 350\omega_{pi}^{-1}$, a density compression in front of the magnetic piston is formed [Fig. 6 (right), solid black line]. This density jump is a steady state shock structure, moving away from the magnetic piston.[10] This forward shock moves at speed $v_f^* = v_0/3.5$ in the center of mass reference frame, where the index f refers to the forward shock.

The upstream velocity in the forward shock frame is

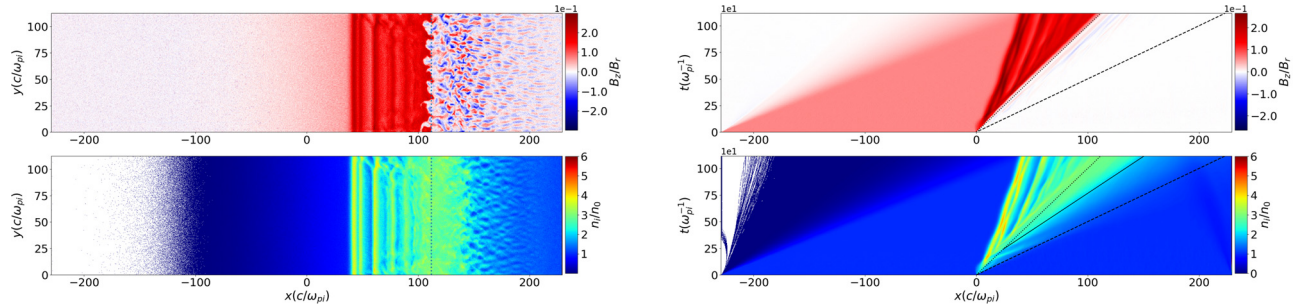

FIG. 8. Magnetic field (top) and ion density (bottom, clamped at 6 for visualization reasons) at time $t = t_{max} = 1118\omega_{pi}^{-1}$ (left) and their evolution with time (right). The speeds v_f, v_c, and v_0 are overplotted by solid, dotted, and dashed lines, respectively. The mass ratio is $\mu = 20$.

$$v_{\rm us}^{f} = |v_{\rm f}^{*} + v_{\rm c}|, \tag{16}$$

leading to an acoustic Mach number $M_{\rm s,f} = v_{\rm us}^{f}/c_{\rm s} = 11v_0/14c_{\rm s} \sim M_{\rm s,r}$. The shock is supercritical as demonstrated in Fig. 7(e). A large fraction of ions of Plasma 2 is reflected at the forward shock potential jump in the interval $20c/\omega_{pi} < x^{*} < 40c/\omega_{pi}$. The density compression near the shock front is $\Delta_{\rm f} \sim 2.8$, whereas the magnetic field is zero in average. This value is in agreement with Eq. (15) considering Alfvénic Mach number $M_{\rm A,f} \to \infty$.

At $t_{\rm max}$, the forward shock front is located at $x^{*} \sim 16c/\omega_{pi}$ and the width of the shock ramp is $\sim 30c/\omega_{pi}$ as it is shown in Fig. 7(f). This value is still much smaller than the ion isotropization length given by Eq. (12).

The anisotropy of Plasma 2 at the shock front is $a_{i2} \sim 1.4$ [solid line in Fig. 7(f)] and goes down to ~ 0.5 at the discontinuity, which is below the limit of $a_i = 1$ mentioned previously.[33]

B. Later shock propagation ($\mu = 20$)

Further shock evolution has been studied in a simulation with mass ratio $\mu = 20$, allowing us to trace the process on the time 10 times longer than that with the real mass ratio. Figure 8 (left) displays the magnetic field amplitude and the proton density at the end of simulation $t = t_{\rm max} = 1118\omega_{pi}^{-1}$ in the interval $-1052/\sqrt{\mu} \le x/(c\omega_{pi}^{-1}) \le 1052/\sqrt{\mu}$.

1. Reverse shock

A fast magnetosonic reverse shock is formed at $t_{\rm r} \simeq 115\omega_{pi}^{-1}$, in agreement with Eq. (11), and moves at the speed $v_{\rm r}^{*} = -v_0/3$ in the center of mass reference frame. The shock parameters are approximately the same as in the previous simulations with a larger mass ratio. The shock is supercritical within $M_{\rm s,r} = 5v_0/6c_{\rm s} \simeq 0.86\sqrt{\mu} \simeq 3.9$ and $M_{\rm A,r} = 12 > M_c = 2.3$. Density and magnetic field jumps near the shock front are characterized by a factor $\Delta_{\rm r} \sim 2.6$, in agreement with Eq. (15). The shock self-reforms on a time period $\sim 2t_{\rm p} \simeq 340\omega_{pi}^{-1}$, forming a double layer at its front.

The electron temperature, magnetic field strength, and ion density in the reverse downstream shock region increase by a factor $\Delta_{\rm r}$, and therefore, the lower-hybrid frequency is $\omega_{LH}^{DS} \simeq 0.1\omega_{pi}$, larger than in the upstream region (cf. Table I). The warm electromagnetic lower-hybrid wave dispersion relation in the downstream region can be written as[39]

$$\omega^2 = \frac{\omega_{LH}^2}{1+K^{-2}}\left[1 + WK^2\frac{v_{Te}^2}{B_0^2}\right], \tag{17}$$

where $K = k^2c^2/\omega_{pe}^2$ and

$$W = 3\frac{T_i}{T_e}(1+K^{-2}) + \frac{1}{2K^2} + \frac{9}{2} - \frac{15+21K^{-2}}{4(1+K^{-2})}. \tag{18}$$

The lower-hybrid wavelength in the simulation $\lambda_x \sim 14c\omega_{pi}^{-1}$ corresponds to the wavenumber $k_x = 2\pi/\lambda_x \simeq 0.45\omega_{pi}/c$. In the downstream reference frame, the reverse shock velocity is $v_{\rm r}^{\rm ds} = v_{\rm us}^{\rm r}/\Delta_{\rm r} \simeq 0.065c$. The lower-hybrid wave moves with a near shock velocity, and its frequency $\omega = k_x v_{\rm sh}^{\rm r} = 0.03\omega_{pi}$ is close to the theoretical value $\omega \simeq 0.035\omega_{pi}$ from Eq. (17). These waves propagate downstream due to the concave dispersion relation in a perpendicular magnetic field.[36,40]

2. Forward shock

Forward shock characteristics are in agreement with the simulations with a larger mass ratio. After an initial transient phase formed at $t_{\rm p}$, the shock is created at $t_{\rm f} \simeq 240\omega_{pi}^{-1}$ and moves with velocity $v_{\rm f}^{*} \simeq v_0/4.5$ in the center of mass reference frame. The shock is supercritical within an acoustic Mach number $M_{\rm s,f} \simeq 13v_0/c_{\rm s}18 \sim 0.75\sqrt{\mu} \simeq 3.35$. The density jump near the shock front is $\Delta_{\rm f} \sim 2.5$ as predicted by Eq. (15) considering an Alfvénic Mach number $M_{\rm A,f} \to \infty$ at the corresponding time moment $t_{\rm max}$ (cf. Fig. 8 right). Merging filaments in the downstream region generate spatial modulations of magnetic field at the scale $\lambda_y \simeq 2\lambda_{\rm sat} \simeq 6c\omega_{pi}^{-1}$. The density in the forward shock downstream region increases to $n_i \sim 2.9n_0$ according to the Rankine–Hugoniot conditions. The remnant Plasma 1 jet, which propagates through the ambient medium, contributes to increase the upstream density to ~ 1.15 (cf. Fig. 9), conserving the density jump $\Delta_{\rm f} \sim 2.5$ according to Eq. (15). At that time, the forward shock is already mediated by the ambient medium, and the decrease in the anisotropy $a_{i2} \to 0$ is only due to filament merging. The spatial scale of magnetic field inhomogeneities reaches eventually a wavelength $\lambda_y \simeq 4\lambda_{\rm sat} \simeq 12c\omega_{pi}^{-1}$ in the shock downstream region as it is shown in Figs. 9(a) and 9(b) in the interval $0 < x^{*} < 36c/\omega_{pi}$.

The forward shock is, thus, at this moment purely electromagnetic, and its width has increased to $\sim 110c\omega_{pi}^{-1}$, reaching an isotropization length, in agreement with Eq. (12). However, the shock has been formed earlier at time $t_{\rm f} < t_{\rm W}$, indicating that the magnetic

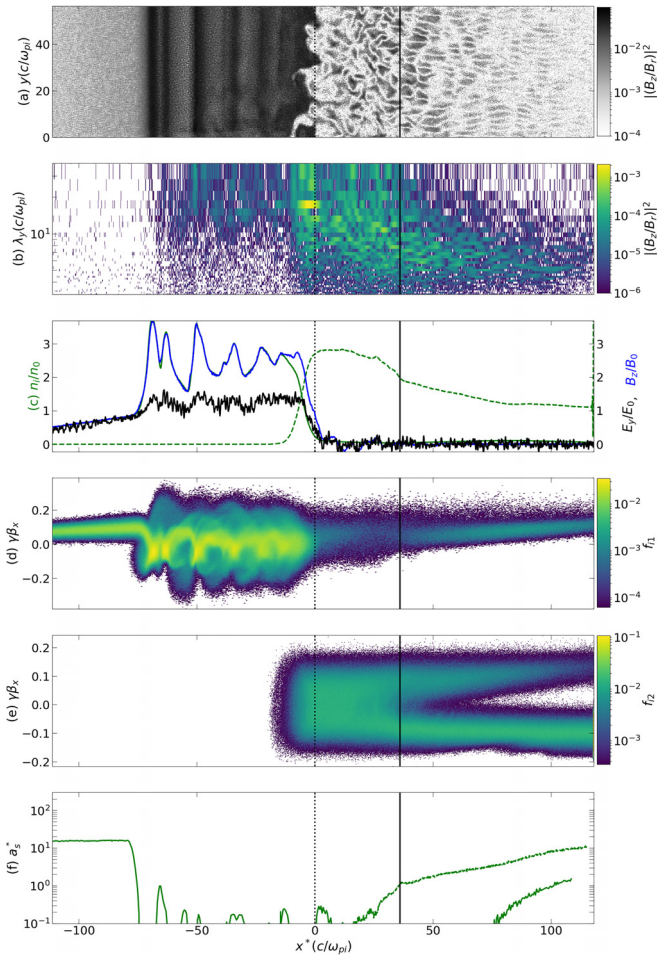

FIG. 9. (a) and (b) The magnetic energy density and its spectrum, respectively. (c) The ion density (green), magnetic field (blue), and electric field (black) averaged over the *y*-axis. (d) and (e) The ion phase space $\gamma\beta_x$ for *i*1 and *i*2. (f) The ion anisotropy. Solid lines correspond to *i*1 and the dashed lines to *i*2. The mass ratio is $\mu = 20$, the time $t = t_{max} = 1118\omega_{pi}^{-1}$, and the reference frame is the center of mass $x^* = x - v_c t$.Vertical dotted and solid lines show the positions $x = v_c t$ and $x = v_f(t - t_f)$, respectively.

piston accelerates the electromagnetic shock formation by reducing sharply the ambient ion anisotropy over a distance of their Larmor radius.

The tangential discontinuity, which balances the total pressure between the two downstream shock regions [cf. Fig. 9(c)], is fully formed. Furthermore, the magnetic mirror edge instability is found to be responsible for the deformation of the discontinuity and for the formation of large magnetic bubbles, reaching a wavelength $\lambda_y \simeq 8\lambda_{sat}$ in the reverse shock downstream region [cf. Figs. 9(a) and 9(b)].

V. DISCUSSION

A. Particle acceleration and heating

Collisionless shocks can heat the plasma and accelerate particles via several mechanisms, making them very relevant in astrophysics. By using the test particle approach, we study the motion of selected particles in prescribed fields. Figures 10(a) and 10(d) display the trajectories of the most energetic test particles obtained for the simulation with $\mu = 50$.

1. Reverse shock

Collisionless perpendicular shocks can reflect particles and heat them via the lower-hybrid wave modes. The Shock Drift Acceleration (SDA) of electrons and protons in the reverse shock downstream region is shown in Figs. 10(a) and 10(d), respectively. The $\mathbf{E} \times \mathbf{B}$ drift moves electrons and positively charged ions in the same direction,[37] but PIC simulations show that ion acceleration is inefficient compared to electromagnetic turbulent shocks, and no particle acceleration has been measured experimentally.[14] Figure 11 (top) shows the electron spectrum. A departure of the cutoff region at t_{max} (blue) from the Maxwellian distribution (black-dashed line) indicates a little acceleration. The electron maximum energy is smaller for lower values of μ, as one can see in subpanel (c) where we compare the spectrum cutoffs for $\mu = 50$ (blue) and 20 (red).

2. Forward shock

Protons perform one cycle shock crossing (from upstream to downstream and back to the upstream). In the shock frame, the energy gain in one cycle for a proton with initial Lorentz factor γ_0 is

$$\frac{\gamma_{cycle}}{\gamma_0} = \frac{1 + \beta_{u,x} v_f/c}{1 + \beta_{d,x} v_f/c}, \tag{19}$$

where $v_f = v_0/5 + v_0/2 = 0.14c$ is the velocity of the forward shock in the laboratory frame (i.e., the forward shock upstream region) and $\beta_{u/d,x}$ is the velocity of the particle in the upstream/downstream region in the *x*-direction.[7] For the particular case shown in Fig. 10, $\beta_{u,x} = 0.021$ and $\beta_{d,x} = -0.24$, giving $\gamma_{cycle}/\gamma_0 = 1.028$ coincident with the simulation result where $\gamma_{cycle}/\gamma_0 = 1.030/1.00\,075 = 1.029$. This estimation suggests that we observed the first cycle of ion acceleration. We note, however, that the scale length of the Weibel turbulence is too small to efficiently scatter the test protons. (Efficient scattering needs magnetic structures of the order of the particle Larmor radius.)

In the forward shock downstream region, the energy of the two representative electrons shown in Fig. 10(a) increased by a factor $\gamma_e/\gamma_0 \sim 1.36$ and 1.51 on a timescale $t_{max} = 70\omega_{pi}^{-1}$. This energy gain can be explained by the second order Fermi process with a characteristic timescale,

$$t_{acc} \sim \frac{3}{4 - \alpha} \left(\frac{c}{u}\right)^2 \left(\frac{\lambda}{c}\right), \tag{20}$$

where u is the velocity of scattering centers and $\lambda \propto \gamma_e^{\alpha}$ is the electron mean-free path in the turbulence (e.g., Ref. 41). In Weibel turbulence, $\lambda \sim r_e^2/s$, where $s > c/\omega_{pi}$. For a relativistic electron with Lorentz factor γ_e, the Larmor radius is $r_e \propto \gamma_e$, and therefore, $\alpha = 2$. By setting $B = 0.2B_r$ (see Fig. 6), we find that during the simulation time, electrons can attain a Lorentz factor γ_e when the velocity of the scattering centers is $u/c \sim 0.02\gamma_e\sqrt{c/s\omega_{pi}}$. Electrons in Fig. 10(a) reach $\gamma_e = 1.398$ and 1.5366 in t_{max}, giving $u \sim 0.03c\sqrt{c/s\omega_{pi}}$ in both cases. This value is consistent with our rough estimation $u \sim \delta(k_{sat})/$

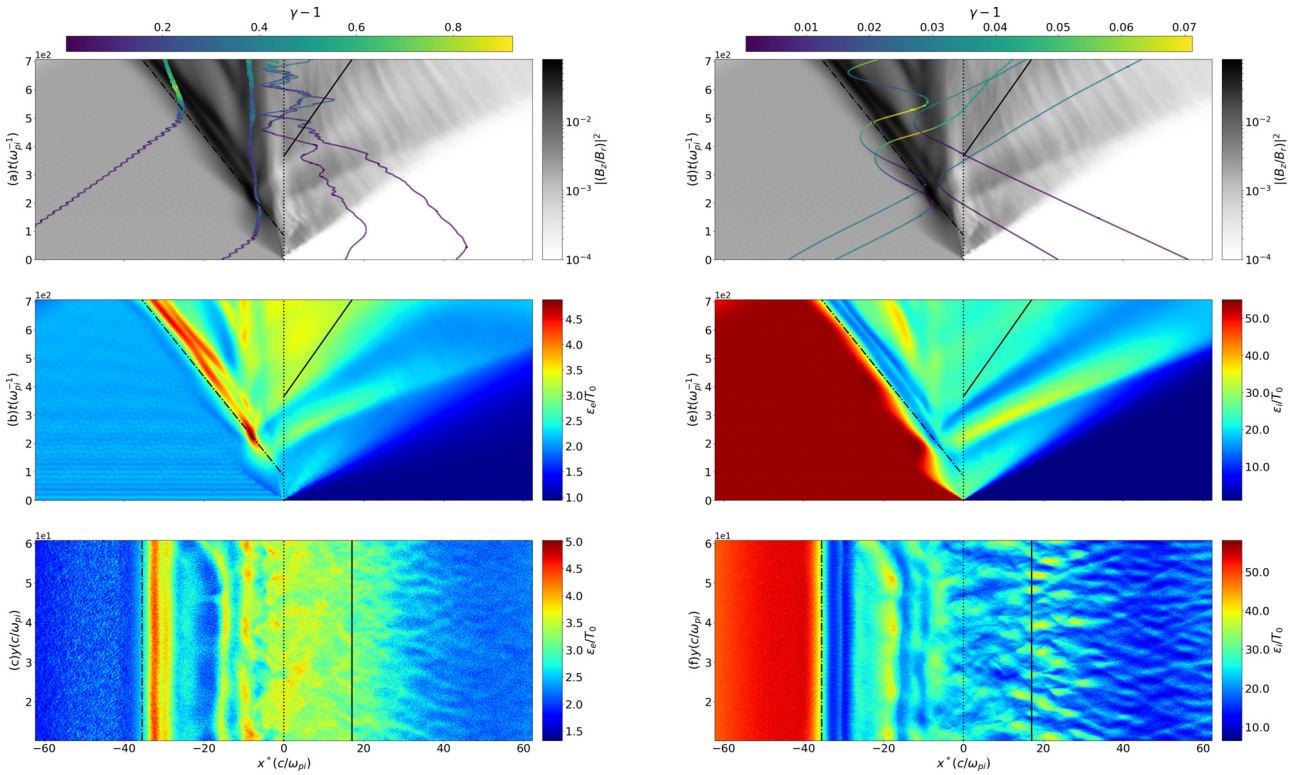

FIG. 10. (a) and (d) The magnetic energy density and the test particle trajectory for four electrons (a) and protons (d) from Plasma 1 and 2. (b) and (e) The time evolution of the particle energy $\epsilon_{e,i}$ integrated over the y-axis. The speeds v_r^*, v_c^*, and v_f^* are overplotted by dash-dotted, dotted, and solid lines, respectively. (c) and (f) The particle energy $\epsilon_{e,i}$ space profile at time $t = t_{max} = 707\omega_{pi}^{-1}$, and the vertical lines show $(t - t_r)v_r^*$, $tv_c^* = 0$ and $(t - t_f)v_f^*$. The mass ratio is $\mu = 50$, and the reference frame is the center of mass $x^* = x - v_c t$.

$k_{sat} \sim 0.007c$ when $s \sim 20c/\omega_{pi}$. The spectrum of electrons is shown in Fig. 11 (bottom), with no significant acceleration at supra-thermal energies. A simulation much longer than the present one is needed for the development of a high-energy tail.

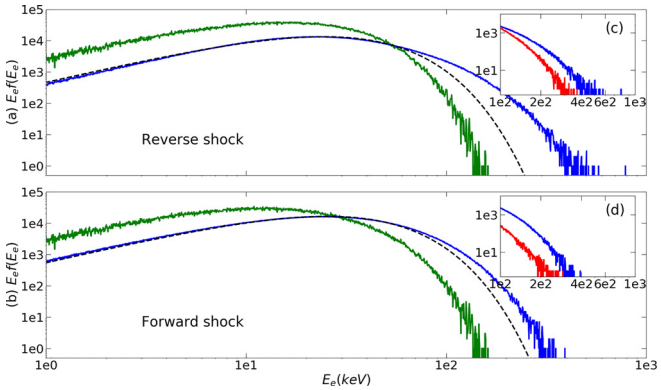

FIG. 11. Electron spectrum in a $70(c/\omega_{pe})$-wide slice, at $x = 50$ and $90c/\omega_{pi}$, in the reverse (a, top) and forward (b, bottom) shock downstream regions at $t_{max} = 707\omega_{pi}^{-1}$ (blue), with a 2D Maxwellian fit (black dashed line). The electron spectra of Plasma 1 and Plasma 2 at $t = 0$ (green) are plotted in (a) and (b), respectively. The mass ratio is $\mu = 50$. For comparison, (c) and (d) show the spectrum cutoff at $t = 707\omega_{pi}^{-1}$ for $\mu = 50$ (blue) and 20 (red).

B. Reduced mass ratio

In the present study, we show that the perpendicular geometry of the magnetic field speeds up the shock formation. In order to reduce the computational cost of the PIC simulations, we accelerated the development of the instabilities and the shock formation by choosing a reduced ion-to-electron mass ratio μ. Reduction of μ has the following consequences:

- The growth rate of the Weibel instability increases[42] accelerating the electromagnetic shock formation [cf. Eq. (13)]. Magnetic field strength and time needed for the ions from Plasma 1 to rotate in the magnetic piston are reduced [cf. Eq. (11)]. However, we succeed to preserve the ratio of the Weibel-mediated shock time formation t_w to the time of ion rotation in the magnetic piston t_p. Figure 12 shows the dependence of this ratio on the ion velocity v_0/c and the magnetic field B_3/B_r. A constant of the ratio t_p/t_w confirms that all four simulations with different ion masses address the same physical situation.
- Reduction of ion mass affects the acoustic, Alfvénic, and magnetosonic velocities, which scale as $\propto 1/\sqrt{\mu}$ but the β parameter remained unchanged (see Table I). The shock speed variation regarding the decrease of the mass ratio from 50 to 20 is only ∼5% (cf. Table II). This is much less than the variation of the acoustic, Alfvénic, and magnetosonic velocities (∼60%). The shock's Mach numbers decrease with the mass ratio by a factor

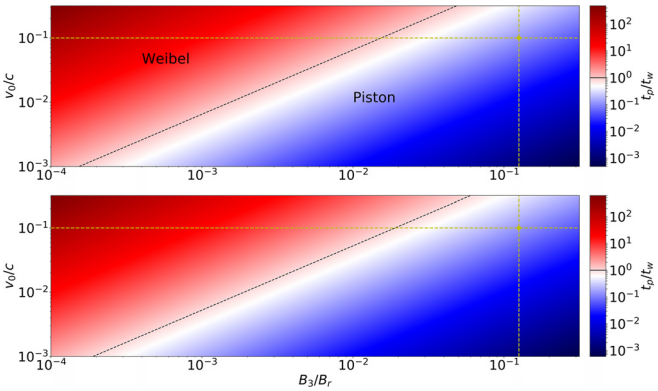

FIG. 12. Ratio of the two time shock formation t_p/t_W as a function of ion velocity v_0/c and magnetic field B_3/B_r. Ion-to-electron mass ratios are $\mu = 20$ (top) and $\mu = 1836$ (bottom). Yellow dots correspond to the simulations presented in this paper.

$\sim\sqrt{\mu}$. However, both shocks remain supercritical in spite of the mass ratio reduction from $\mu = 1836$ to 20, so all four simulations address the physically similar conditions. The $\sqrt{\mu}$ scaling of the characteristic times and dimensions is in agreement with results shown in Figs. 4, 6, and 8 (bottom), where each step of the shock formation remains unchanged. This fact has been verified by comparing the results obtained in a downscaled simulation at the time moment corresponding to the end of simulation with a larger ion mass.

- Figures 11(c) and 11(d) indicate that the electron energy cutoff increases for larger values of μ. Therefore, in the simulations with a reduced ion mass, the apparent electron energy is smaller than it would be in the case with a real ion mass.

VI. CONCLUSIONS

We performed a numerical study of shock formation and propagation with a 2D PIC code. A mildly relativistic magnetized jet moving in a nonmagnetized ambient medium creates a double shock structure where the forward shock is mediated by Weibel turbulence and the reverse shock is mediated by lower-hybrid waves. Note here that the Weibel instability is not generated in the magnetized plasma as in Refs. 43 and 44. The downstream shock regions are separated by a tangential discontinuity. To our knowledge, this configuration of shocks was not considered in previous studies. Long-time shock evolution is assessed by a progressive reduction of the ion mass.

The jet magnetic field creates a magnetic piston, which initiates a transient phase where upstream particles are reflected by the magnetic wall. In contrast to other simulations with an artificial reflecting boundary (see e.g., Ref. 10), this magnetic wall is real and can be reproduced in experiments. The supercritical reverse magnetized shock forms by the jet ions reflected from the piston at t_p. The forward shock forms after the transient stage as a hybrid structure where the magnetic piston and the Weibel turbulence dissipate the upstream kinetic energy. The time formation of this hybrid shock structure can be compared to the case where the shock is only Weibel-mediated,[34] with no magnetic field carried by the jet. It appears that the magnetic piston has accelerated the forward shock formation by $t_w/t_f \simeq 4.8$ for any mass ratio (cf. Table II). Furthermore, large simulation time reveals that after the forward shock is detached from the piston, it becomes purely Weibel-mediated.

TABLE II. List of shock speeds in the laboratory reference frame (in c units), associated Mach numbers and characteristic times (in $1/\omega_{pi}$ units) for the simulations with $\mu = 50$ and 20.

μ	$\lvert v^r_{us}\rvert$ [c]	$\lvert v^f_{us}\rvert$ [c]	$M_{s,r}$	$M_{A,r}$	$M_{s,f}$	$M_{A,f}$	t_p [ω_{pi}^{-1}]	t_f [ω_{pi}^{-1}]	t_w [ω_{pi}^{-1}]
50	0.16	0.16	5.7	18	5.7	∞	180	350	1673
20	0.17	0.14	3.9	12	3.4	∞	115	240	1160

The tangential discontinuity that ensures the pressure equilibrium between the forward and reverse shock downstream regions is destabilized by a mirror instability,[38] generating a large spatial modulation. The discontinuity could eventually break in a longer timescale, leading to a large wavelength turbulence.

Particle acceleration by a turbulence in astrophysical shocks is of great importance for understanding the nonthermal universe. In particular, the synchrotron radio emission detected in the termination region of active galactic nuclei, microquasars, and protostellar jets indicates the presence of relativistic electrons. Electrons and protons can be accelerated in the termination shocks and in the turbulent shock downstream region through Fermi I and Fermi II mechanisms, respectively. PIC simulations are a unique tool for assessing kinetic processes relevant for particle acceleration. Our simulations show that particles gain energy during the simulation time. The energy gain of electrons ($\gamma_e/\gamma_0 \sim 1.4$ and 1.5) can be explained by their diffusion in the Weibel turbulence downstream of the forward shock. This is the Fermi II process shown in Fig. 10(a). However, the scale length of Weibel turbulence is not large enough to efficiently accelerate ions [see Fig. 10(d)]. Although the ion energy gain ($\gamma_i/\gamma_0 \sim 1.03$) can be explained by shock crossing [see Eq. (19)], the duration of our simulations is not sufficient for assessing the ion acceleration mechanism.

PIC calculations provide also the framework for connecting laboratory experiments with astrophysical studies. Laboratory experiments on electromagnetic collisionless shocks are formidably difficult to conduct since they have to meet critical shock properties in astrophysical regimes such as magnetization and low collisionality and they have to be super-Alfvénic.[45,46] They require matter under extreme conditions and must satisfy the strict condition $\lambda_i \gg L_{sys} \gg L_{iso}$, where L_{sys} is the system size and λ_i is the ion mean free path.[47] The latter means that these shocks require that the flows are highly collisionless and also that the ion anisotropy decreases fast enough before the plasma reaches the bounds of the experiment. The acceleration of the electromagnetic shock formation due to a magnetic piston could be a way to achieve the formation of such shocks in laboratory experiment. This method has been tested by Ref. 18 and will require further experiments for studying a long-term shock evolution in the laboratory environment.

ACKNOWLEDGMENTS

This work was also granted access to the HPC resources of CINES and TGCC under allocations Nos. A0020510052 and A0030506129 made by GENCI (Grand Equipment National de Calcul Intensif) and partially supported by the 2015–2019 grant of

the Institut Universitaire de France. This work was also supported by the MEPhI Academic Excellence Project (Contract Nos. 02.a03.21.0005 and 27.08.2013) and access to MEPhI HPC resources. This work was supported by the project advanced research using high intensity laser produced photons and particles (ADONIS) (No. *CZ*.02.1.01/0.0/0.0/$16_0$19/0000789) and by the project High Field Initiative (HiFI) (No. *CZ*.02.1.01/0.0/0.0/$15_0$03/0000449), both from the European Regional Development Fund. We also acknowledge the financial support from Project LQ1606 of the Ministry of Education, Youth, and Sports as a part of targeted support from the National Programme of Sustainability II. Q.M. and A.T.A. thank the Czech Science Foundation for support under Grant No. GAČR 20–19854S.

DATA AVAILABILITY

The data that support the findings of this study are available from the corresponding author upon reasonable request.

REFERENCES

[1]D. W. Forslund and C. R. Shonk, "Formation and structure of electrostatic collisionless shocks," Phys. Rev. Lett. **25**, 1699–1702 (1970).
[2]M. A. Balikhin, M. Nozdrachev, M. Dunlop, V. Krasnosel'skikh, S. N. Walker, H. S. C. K. Alleyne, V. Formisano, M. Andre, A. Balogh, A. Eriksson, and K. Yearby, "Observation of the terrestrial bow shock in quasi-electrostatic subshock regime," J. Geophys. Res. **107**, SSH 1-1–SSH 1-9, https://doi.org/10.1029/2001JA000327 (2002).
[3]M. Opher, J. F. Drake, B. Zieger, M. Swisdak, and G. Toth, "Magnetized jets driven by the sun: The structure of the heliosphere revisited-updates," Phys. Plasmas **23**, 056501 (2016).
[4]M. V. Medvedev and A. Loeb, "Generation of magnetic fields in the relativistic shock of gamma-ray burst sources," Astrophys. J. **526**, 697 (1999).
[5]Y. Lyubarsky and D. Eichler, "Are gamma-ray burst shocks mediated by the Weibel instability?," Astrophys. J. **647**, 1250 (2006).
[6]A. Marcowith, A. Bret, A. Bykov, M. E. Dieckmann, L. O. Drury, B. Lembège, M. Lemoine, G. Morlino, G. Murphy, G. Pelletier, I. Plotnikov, B. Reville, M. Riquelme, L. Sironi, and A. S. Novo, "The microphysics of collisionless shock waves," Rep. Prog. Phys. **79**, 046901 (2016).
[7]A. R. Bell, "The acceleration of cosmic rays in shock fronts-I," Mon. Not. R. Astron. Soc. **182**, 147–156 (1978).
[8]R. D. Blandford and J. P. Ostriker, "Particle acceleration by astrophysical shocks," Astrophys. J. Lett. **221**, L29–L32 (1978).
[9]E. S. Weibel, "Spontaneously growing transverse waves in a plasma due to an anisotropic velocity distribution," Phys. Rev. Lett. **2**, 83–84 (1959).
[10]A. Spitkovsky, "On the structure of relativistic collisionless shocks in electron-ion plasmas," Astrophys. J. Lett. **673**, L39 (2008).
[11]A. Spitkovsky, "Particle acceleration in relativistic collisionless shocks: Fermi process at last?," Astrophys. J. Lett. **682**, L5 (2008).
[12]H. Takabe, T. N. Kato, Y. Sakawa, Y. Kuramitsu, T. Morita, T. Kadono, K. Shigemori, K. Otani, H. Nagatomo, T. Norimatsu, S. Dono, T. Endo, K. Miyanishi, T. Kimura, A. Shiroshita, N. Ozaki, R. Kodama, S. Fujioka, H. Nishimura, D. Salzman, B. Loupias, C. Gregory, M. Koenig, J. N. Waugh, N. C. Woolsey, D. Kato, Y. Li-T, Q.-L. Dong, S.-J. Wang, Y. Zhang, J. Zhao, F. Wang-L, H. Wei-G, J.-R. Shi, G. Zhao, J. Zhang-Y, T.-S. Wen, W.-H. Zhang, X. Hu, S.-Y. Liu, Y. K. Ding, L. Zhang, Y.-J. Tang, B.-H. Zhang, Z.-J. Zheng, Z.-M. Sheng, and J. Zhang, "High-Mach number collisionless shock and photo-ionized non-LTE plasma for laboratory astrophysics with intense lasers," Plasma Phys. Controlled Fusion **50**, 124057 (2008).
[13]H. Ahmed, M. E. Dieckmann, L. Romagnani, D. Doria, G. Sarri, M. Cerchez, E. Ianni, I. Kourakis, A. L. Giesecke, M. Notley, R. Prasad, K. Quinn, O. Willi, and M. Borghesi, "Time-resolved characterization of the formation of a collisionless shock," Phys. Rev. Lett. **110**, 205001 (2013).
[14]D. B. Schaeffer, W. Fox, D. Haberberger, G. Fiksel, A. Bhattacharjee, D. H. Barnak, S. X. Hu, K. Germaschewski, and R. K. Follett, "High-Mach number, laser-driven magnetized collisionless shocks," Phys. Plasmas **24**, 122702 (2017).
[15]W. Fox, G. Fiksel, A. A. B. P. Y. Chang, K. Germaschewski, S. X. Hu, and P. M. Nilson, "Filamentation instability of counterstreaming laser-driven plasmas," Phys. Rev. Lett. **111**, 225002 (2013).
[16]C. M. Huntington, F. Fiuza, J. S. Ross, A. Zylstra, R. P. Drake, D. Froula, G. Gregori, N. L. Kugland, C. Kuranz, M. Levy, C. K. Li, J. Meinecke, T. Morita, R. Petrasso, C. Plechaty, B. A. Remington, D. D. Ryutov, Y. Sakawa, and A. A. S. H. S. Park, "Observation of magnetic field generation via the Weibel instability in interpenetrating plasma flows," Nat. Phys. **11**, 173–176 (2015).
[17]C. M. Huntington, M. J. E. Manuel, J. S. Ross, S. C. Wilks, F. Fiuza, H. G. Rinderknecht, H. S. Park, G. Gregori, D. P. Higginson, J. Park, B. B. Pollock, B. A. Remington, D. D. Ryutov, C. Ruyer, Y. Sakawa, H. Sio, A. Spitkovsky, G. F. Swadling, H. Takabe, and A. B. Zylstra, "Magnetic field production via the Weibel instability in interpenetrating plasma flows," Phys. Plasmas **24**, 041410 (2017).
[18]C. K. Li, V. T. Tikhonchuk, Q. Moreno, H. Sio, E. D'Humières, X. Ribeyre, P. Korneev, S. Atzeni, R. Betti, A. Birkel, E. M. Campbell, R. K. Follett, J. A. Frenje, S. X. Hu, M. Koenig, Y. Sakawa, T. C. Sangster, F. H. Seguin, H. Takabe, S. Zhang, and R. D. Petrasso, "Collisionless shocks driven by supersonic plasma flows with self-generated magnetic fields," Phys. Rev. Lett. **123**, 055002 (2019).
[19]M. E. Dieckmann, D. Folini, I. Hotz, A. Nordman, P. Dell'Acqua, A. Ynnerman, and R. Walder, "Structure of a collisionless pair jet in a magnetized electron-proton plasma: Flow-aligned magnetic field," Astron. Astrophys. **621**, A142 (2019).
[20]P. Hartigan, "The visibility of the Mach disk and the bow shock of a stellar jet," Astrophys. J. **339**, 987 (1989).
[21]S. Matsukiyo and M. Scholer, "Modified two-stream instability in the foot of high Mach number quasi-perpendicular shocks," J. Geophys. Res. **108**, 010080, https://doi.org/10.1029/2003JA010080 (2003).
[22]H. Sakemi, M. Machida, T. Akahori, H. Nakanishi, H. Akamatsu, K. Kurahara, and J. Farnes, "Magnetic field analysis of the bow and terminal shock of the ss433 jet," Publ. Astron. Soc. Jpn. **70**, 27 (2018).
[23]Y. Sentoku and A. J. Kemp, "Numerical methods for particle simulations at extreme densities and temperatures: Weighted particles, relativistic collisions and reduced currents," J. Comput. Phys. **227**, 6846–6861 (2008).
[24]C. Birdsall and A. Langdon, *Plasma Physics Via Computer Simulation*, Series in Plasma Physics and Fluid Dynamics (Taylor & Francis, 2004).
[25]D. D. Ryutov, N. L. Kugland, H. S. Park, C. Plechaty, B. A. Remington, and J. S. Ross, "Basic scalings for collisionless-shock experiments in a plasma without pre-imposed magnetic field," Plasma Phys. Controlled Fusion **54**, 105021 (2012).
[26]S. G. Bochkarev, E. d'Humières, P. Korneev, V. Y. Bychenkov, and V. T. Tikhonchuk, "The role of electron heating in electromagnetic collisionless shock formation," High Energy Density Phys. **17**, 175–182 (2015).
[27]A. M. Bykov and R. A. Treumann, "Fundamentals of collisionless shocks for astrophysical application, 2. Relativistic shocks," Astron. Astrophys. Rev. **19**, 42 (2011).
[28]R. Z. Sagdeev, D. A. Usikov, and G. M. Zaslavsky, *Nonlinear Physics -From the Pendulum to Turbulence and Chaos* (Harwood Academic Publishers, 1988).
[29]T. D. Arber, K. Bennett, C. S. Brady, A. Lawrence-Douglas, M. G. Ramsay, N. J. Sircombe, P. Gillies, R. G. Evans, H. Schmitz, and A. R. A. B. C. P. Ridgers, "Contemporary particle-in-cell approach to laser-plasma modelling," Plasma Phys. Controlled Fusion **57**, 113001 (2015).
[30]The choice of this code for these simulations is explained by an efficient 1D3V parallelization of EPOCH.
[31]C. Ruyer, L. Gremillet, A. Debayle, and G. Bonnaud, "Nonlinear dynamics of the ion Weibel-filamentation instability: An analytical model for the evolution of the plasma and spectral properties," Phys. Plasmas **22**, 032102 (2015).
[32]R. C. Davidson, D. A. Hammer, I. Haber, and C. E. Wagner, "Nonlinear development of electromagnetic instabilities in anisotropic plasmas," Phys. Fluids **15**, 317–333 (1972).
[33]C. Ruyer, L. Gremillet, G. Bonnaud, and C. Riconda, "Analytical predictions of field and plasma dynamics during nonlinear Weibel-mediated flow collisions," Phys. Rev. Lett. **117**, 065001 (2016).
[34]C. Ruyer, L. Gremillet, G. Bonnaud, and C. Riconda, "A self-consistent analytical model for the upstream magnetic-field and ion-beam properties in Weibel-mediated collisionless shocks," Phys. Plasmas **24**, 041409 (2017).

[35]W. Marshall, "The structure of magneto-hydrodynamic shock waves," Proc. R. Soc. London, Ser. A **233**, 367–376 (1955).
[36]Q. Moreno, M. E. Dieckmann, X. Ribeyre, V. T. Tikhonchuk, D. Folini, R. Walder, and E. d'Humieres, "Failed self-reformation of a sub-critical fast magnetosonic shock in collisionless plasma," Plasma Res. Express **1**, 035001 (2019).
[37]S. Matsukiyo and M. Scholer, "Simulations of pickup ion mediated quasi-perpendicular shocks: Implications for the heliospheric termination shock," J. Geophys. Res. **119**, 2388–2399, https://doi.org/10.1002/2013JA019654 (2014).
[38]P. Korneev, E. d'Humières, and V. T. Tikhonchuk, "Collisionless plasma interpenetration in a strong magnetic field for laboratory astrophysics experiments," Phys. Plasmas **21**, 022117 (2014).
[39]A. L. Verdon, I. H. Cairns, D. B. Melrose, and P. A. Robinson, "Warm electromagnetic lower hybrid wave dispersion relation," Phys. Plasmas **16**, 052105 (2009).
[40]M. E. Dieckmann, Q. Moreno, D. Doria, L. Romagnani, G. Sarri, D. Folini, R. Walder, A. Bret, E. d'Humieres, and M. Borghesi, "Expansion of a radially symmetric blast shell into a uniformly magnetized plasma," Phys. Plasmas **25**, 052108 (2018).
[41]F. M. Rieger, V. Bosch-Ramon, and P. Duffy, "Fermi acceleration in astrophysical jets," Astrophys. Space Sci. **309**, 119–125 (2007).
[42]A. Bret and M. E. Dieckmann, "How large can the electron to proton mass ratio be in particle-in-cell simulations of unstable systems?," Phys. Plasmas **17**, 032109 (2010).
[43]Y. Matsumoto, T. Amano, T. N. Kato, and M. Hoshino, "Stochastic electron acceleration during spontaneous turbulent reconnection in a strong shock wave," Science **347**, 974–978 (2015).
[44]Y. Matsumoto, T. Amano, T. N. Kato, and M. Hoshino, "Electron surfing and drift accelerations in a Weibel-dominated high-Mach-number shock," Phys. Rev. Lett. **119**, 105101 (2017).
[45]R. P. Drake, "The design of laboratory experiments to produce collisionless shocks of cosmic relevance," Phys. Plasmas **7**, 4690–4698 (2000).
[46]R. A. Treumann, "Fundamentals of collisionless shocks for astrophysical application, 1. Non-relativistic shocks," Astron. Astrophys. Rev. **17**, 409–535 (2009).
[47]J. D. Huba, *NRL Plasma Formulary* (Naval Research Laboratory, 2009).